Investigation of the crystal structure and ionic conductivity in the ternary system $(Yb_2O_3)_x$–$(Sc_2O_3)_{(0.11-x)}$–$(ZrO_2)_{0.89}$ ($x = 0$–0.11)

Fang Yuan, Jianxin Wang, He Miao, Cunxin Guo, Wei Guo Wang *

Division of Fuel Cell and Energy Technology, Ningbo Institute of Material Technology and Engineering, Chinese Academy of Sciences, 519 Zhuangshi Road, Ningbo 315201, China

ARTICLE INFO

ABSTRACT

The ternary system $(Yb_2O_3)_x$–$(Sc_2O_3)_{(0.11-x)}$–$(ZrO_2)_{0.89}$ ($x = 0$–0.11) specimens have been prepared using a co-precipitation method. The properties of this series of samples are affected by the ytterbium element. A stabilized cubic phase is obtained at room temperature by introducing ytterbium and the unit cell parameters show a linear increasing relationship with content of Yb_2O_3, which also contributes to abatement of the conductivity from 0.099 S/cm to 0.020 S/cm at 800 °C. However, the conductivity tends to remain a constant at lower temperatures ranging from 500 °C to 650 °C as the addition of Yb_2O_3 is reduced to below 3 mol%, achieving high up to 0.015 S/cm at 650 °C for a 3Yb8ScSZ body, indicating a potential to be utilized as an electrolyte material for intermediate temperature solid oxide fuel cells.

1. Introduction

Solid oxide fuel cells (SOFCs), as a highly efficient and clean power generation device, have been demonstrated in a broad range of applications from small auxiliary power units to large scale power plants [1,2]. Lowering operational temperatures is one of the critical points to cut down the cost and has obtained increased attentions recently, which can mainly lead to enhancement of the cell stability and extension of cheaper materials selection for interconnection. Therefore, it is significant to develop new electrolyte materials with higher ion conductivities at low temperatures. The solid materials have been investigated as the electrolytes of solid oxide fuel cells including zirconia-, ceria- and lanthanum gallate-based materials. Scandia stabilised zirconia (ScSZ) shows the highest conductivity among the zirconia systems. The high conductivity of ScSZ is attributed to the small mismatch in size between Zr^{4+} and Sc^{3+}, leading to a smaller energy for defect association between oxygen vacancies and cations, which increases mobility and conductivity. Nevertheless, ScSZ materials have two major problems. ScSZ shows a large aging rate if scandia content is too low, but the cubic phase transforms to a rhombohedral phase when scandia content is increased to 10–12 mol%, resulting in a much lower conductivity [3,4]. On the other hand, the high cost of scandia makes it very difficult to be widely employed as an electrolyte material. Substituting the scandia with other oxides is becoming one of the most effective solutions to these problems [5]. Many studies have been performed on the ternary system M_xO_y–Sc_2O_3–ZrO_2. M_xO_y are CeO_2 [6–10], Y_2O_3 [11–15], Yb_2O_3 [3,16], Bi_2O_3 [16–18], Al_2O_3 [19], and Ga_2O_3 [20]. In the Yb_2O_3–Sc_2O_3–ZrO_2 system, the rhombohedral phase could be eliminated when the substitution of Yb_2O_3 was over 2 mol%, and the highest value of ionic conductivity was obtained when the co-doping content reached to 11 mol%, both at 800 °C and 1000 °C. This result indicated that 11 mol% might be the best co-doping level in the Yb_2O_3–Sc_2O_3–ZrO_2 system [3]. However, there is no reports on the best ratio of Yb_2O_3/Sc_2O_3. Yamaji et al. [18] successfully stabilised the cubic phase and obtained a maximum conductivity of 0.30 S/cm and a maximum power density of 210 mW/cm² at 1000 °C for 1Yb8ScSZ by co-doping of Sc_2O_3 and Yb_2O_3 into ZrO_2. But their investigations are only limited to a certain range of Yb_2O_3 from 1 mol% to 2 mol%. In addition, the difference in ionic radius between the dopant and host can play an important role in the conductivity. Better properties are to be expected if the size of dopant cation is close to the host cation. The radius of Yb^{3+} and Sc^{3+} are both close to the Zr^{4+}. Furthermore, Yb is less costly than Sc. In present study, the 11 mol% has been selected as the co-doping level to get the best ratio of Yb_2O_3/Sc_2O. The phase structure and conductivity properties of the $(Yb_2O_3)_x$–$(Sc_2O_3)_{(0.11-x)}$–$(ZrO_2)_{0.89}$ ($x = 0$–0.11) system are mainly investigated to manifest the changes of crystal structure and conductivity with Yb_2O_3 addition. A good composition is explored, which is free of rhombohedral phase, own acceptable conductivity at relatively low temperature and contains low content of Sc_2O_3.

* Corresponding author. Tel.: +86 574 87911363; fax: +86 574 87910728.
  E-mail address: wgwang@nimte.ac.cn (W.G. Wang).

2. Experiments

Powders of $Zr(NO_3)_4$ (Aladdin, 99.99%), Yb_2O_3 (Sinopharm Chemical Reagent Co. 99.99%) and Sc_2O_3 (Beijing Founder Star Science & Technology Co. 99.99%) were selected as starting experimental materials to prepare target materials using a co-precipitation method. Firstly, stoichiometric Yb_2O_3 and Sc_2O_3 were dissolved into nitric acid and the solution was heated and continuous stirred until a clear solution was obtained. The $Zr(NO_3)_4 \cdot 5H_2O$, meanwhile, was dissolved in the distilled water at room temperature. The two solutions were then blended to yield the stock solution. Precipitation was carried out by adding the stock solutions to a vigorously stirred ammonia solution. The pH value of the final solution was adjusted at over nine after precipitation. The precipitation was thoroughly washed with the distilled water and ethanol until most of the ammonia and water were eliminated by vacuum filtration. Finally, the co-precipitated hydroxides were dried at 80 °C for 12 h and then calcined at 800 °C for 2 h in air. The powders were uniaxially pressed into discs with a diameter of 8 mm and a thickness of 1–2 mm with polyvinyl alcohol (PVA) as the binder under 300 MPa. The pellets were sintered at 1550 °C for 10 h in air. Nomenclature, compositions and densities of the various specimens has been characterized and listed in Table 1.

The phase structures of powders and the sintered pellets were confirmed using the X-ray-diffraction (XRD, Bruker D8 Advance, Germany) technique, and the measurement was proceeded with Cu $K_\alpha1$ radiation ($\lambda = 0.1542$ nm) at a step of 0.02°/s in the Bragg angle (2 theta) range from 20° to 90°. In-situ high temperature XRD was also conducted with a heating rate of 0.2 °C/s to investigate the phase transition ranging from room temperature to 1000 °C. The detection limit of XRD is approximately 1%. The microstructures of sintered pellets were analyzed using a Field Emission Scanning Electron Microscopy (FE-SEM, Hitachi, S-4800, Japan). The specimen density was calculated from the pellet geometry and mass. The theoretical density was derived from the lattice parameters obtained from the XRD diffraction pattern.

For the conductivity measurement, the pellets were coated with platinum paste on both sides as electrodes and sintered at 950 °C for 3 h. Impedance measurements were performed using a frequency response analyser (FRA, Solartron 1260). The measuring frequency range was from 10 MHz to 0.1 Hz with an interruption potential of 0.5 V. The heating program was set from 300 °C to 900 °C with an interval of 50 °C in air. The impedance data were collected by Zviewer software. The ionic conductivity σ was calculated based on the impedance data, and the activation energy E_a of the conductivity was determined by the Arrhenius law.

3. Results and discussion

All the samples were examined by X-ray fluorescence (XRF), and the results confirmed the compositions. The typical SEM pictures of 1Yb10ScSZ and 2Yb9ScSZ pellet surfaces were shown in Fig. 1. The microstructures of other compositions are similar to these two compositions. As showed in the pictures, the electrolytes are dense. The particles are all closely contacted except for few of closed pores. All these indicate the good electrolyte microstructure. The relative densities were obtained, reaching up to 73–92%. The theoretical densities increased with the increase of Yb content.

4. Characterization of crystal structure

Fig. 2 showed the XRD patterns of the pellets after sintering at 1550 °C for 10 h. The cubic phase had been obtained as the main phase for most samples, but the 11ScSZ, 1Yb10ScSZ, 4Yb7ScSZ and 6Yb5ScSZ compositions were mixed by the rhombohedral and cubic phases. For the 4Yb7ScSZ and 6Yb5ScSZ compositions, which contained a small amount of rhombohedral phase, we repeated the synthesis process, and the results showed that it was likely to form the rhombohedral phase in those compositions, but they were almost purely cubic phase. It was reported that the formation of rhombohedral phase was related to content of the scandia element in Sc_2O_3-ZrO_2 system [21], which can be restrained by adding a secondary oxide dopant [3,6–20,22]. That was further confirmed by results of the XRD examination in our study. single cubic phase can be obtained when the Yb_2O_3 content came to higher than 2 mol%, and the phase compositions were basically in agreement with the results in Ref. [3], where the author found that the rhombohedral phase can be avoided when the addition of Yb_2O_3 was more than 2 mol%.

11ScSZ always contained the rhombohedral phase and the phase transition temperature was reported to be around 600–650 °C [3,20]. The phase transition temperature from the rhombohedral phase to cubic phase decreased by the substitution of Al [19], Ga [20], and Bi [17]. In our study, 11ScSZ and 1YbScSZ were in a mixture of cubic phase and rhombohedral phase. The in-situ high temperature XRD patterns for 1Yb10ScSZ were shown in Fig. 3. The peaks of the rhombohedral phase disappeared when the temperature reached 500 °C, which indicated that the rhombohedral phase transitioned into the cubic phase from approximately 450 °C to 500 °C. Comparing with 11ScSZ, the 1Yb10ScSZ composition demonstrated a decrease of phase transition temperature by nearly 150 °C. Thus, replacing the Sc_2O_3 by Yb_2O_3 for 11ScSZ can lower the rhombohedral phase transformation temperature and even stabilise the cubic phase at room temperature when the content of Yb_2O_3 exceeding 2 mol%. The mechanism of the cubic stabilization was not established until now. The strain in the crystalline induced by adding a secondary oxide with the different radius to the Sc^{3+} was concerned [19].

The ionic radii of Yb^{3+} and Sc^{3+} were 0.858 Å and 0.745 Å, respectively. The ionic radius of Yb^{3+} was larger than that of Sc^{3+}. Therefore, an increase of the unit cell parameter can be expected when the Sc cation was substituted by Yb. The unit cell parameters were calculated according to the patterns of XRD diffraction. The specified value of the unit cell parameters for all of the compositions were shown in Table 1. The unit cell parameter of 11YbSZ was 5.13 Å. Compared to 11ScSZ of 5.08 Å, there was a remarkable increase of the unit cell parameter. The dependency of unit cell parameter on Yb_2O_3 content was shown in Fig. 4. This increase was almost linear in the range from 0 to 11 mol% ytterbium, which also implied that all of the Sc cations were substituted by Yb. According to the unit cell parameters obtained for all compositions, the theoretical densities and relative densities were calculated as listed in Table 1.

4.1. Conductivity dependency

The electrical conductivities of the system were studied by the impedance spectroscopy. These measurements were composed of

Table 1
Nomenclature, densities and unit cell parameters of compositions in$(Yb_2O_3)_x$ –$(Sc_2O_3)_{(0.11-x)}$–$(ZrO_2)_{0.89}$ (x = 0–0.11) system.

| Nomenclature	Compositions	Unit cell parameter (cubic) (Å)	Rhombohedral phase content (wt.%)	Theoretical density (g/cm³)	Specimen density (g/cm³)	Relativity density (%)
11ScSZ	$(Sc_2O_3)_{0.11}(ZrO_2)_{0.89}$	5.08125	12.022	5.70574	5.19779	91.09753
1Yb10ScSZ	$(Yb_2O_3)_{0.01}(Sc_2O_3)_{0.10}(ZrO_2)_{0.89}$	5.08924	32.407	5.79977	5.26794	90.83011
2Yb9ScSZ	$(Yb_2O_3)_{0.02}(Sc_2O_3)_{0.09}(ZrO_2)_{0.89}$	5.09111	0.000	5.89536	5.37237	91.12876
3Yb8ScSZ	$(Yb_2O_3)_{0.03}(Sc_2O_3)_{0.08}(ZrO_2)_{0.89}$	5.09594	0.000	5.99449	5.25794	87.71287
4Yb7ScSZ	$(Yb_2O_3)_{0.04}(Sc_2O_3)_{0.07}(ZrO_2)_{0.89}$	5.10213	0.000	6.08815	5.43139	89.21241
5Yb6ScSZ	$(Yb_2O_3)_{0.05}(Sc_2O_3)_{0.06}(ZrO_2)_{0.89}$	5.10395	0.000	6.19698	5.40542	87.22673
6Yb5ScSZ	$(Yb_2O_3)_{0.06}(Sc_2O_3)_{0.05}(ZrO_2)_{0.89}$	5.10779	0.000	6.29808	5.78987	91.93068
7Yb4ScSZ	$(Yb_2O_3)_{0.07}(Sc_2O_3)_{0.04}(ZrO_2)_{0.89}$	5.11276	0.000	6.39447	5.55094	86.80844
8Yb3ScSZ	$(Yb_2O_3)_{0.08}(Sc_2O_3)_{0.03}(ZrO_2)_{0.89}$	5.11815	0.000	6.48866	5.76831	88.89827
9Yb2ScSZ	$(Yb_2O_3)_{0.09}(Sc_2O_3)_{0.02}(ZrO_2)_{0.89}$	5.12116	0.000	6.59140	5.40542	82.00713
10Yb1ScSZ	$(Yb_2O_3)_{0.10}(Sc_2O_3)_{0.01}(ZrO_2)_{0.89}$	5.12672	0.000	6.68378	5.47017	81.84243
11YbSZ	$(Yb_2O_3)_{0.11}(ZrO_2)_{0.89}$	5.13029	0.000	6.78340	5.00835	73.83241
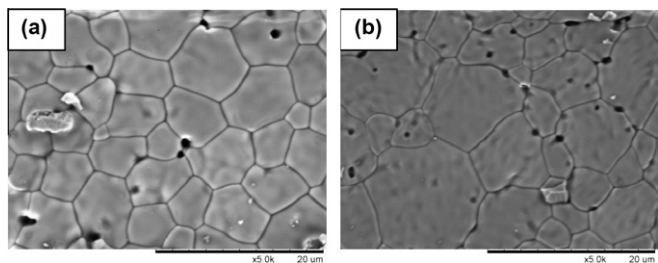
Fig. 1. SEM micrographs of the electrolyte pellet sintered at 1550 °C for 10 h. (a) 1Yb10ScSZ and (b) 2Yb9ScSZ.

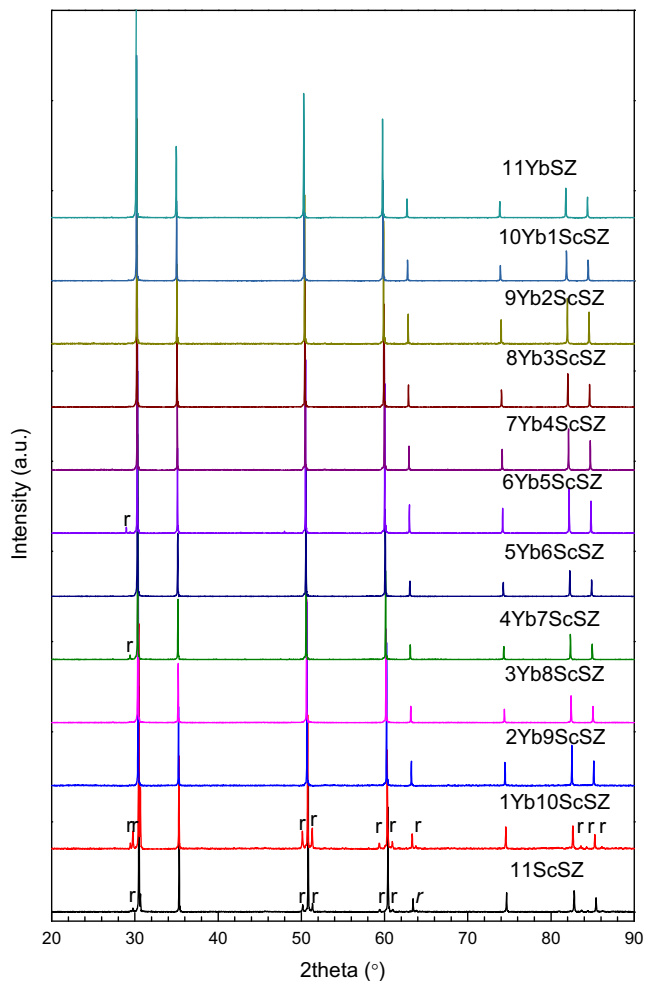**Fig. 2.** XRD patterns of the pellets after sintering at 1550 °C for 10 h, obtained at room temperature (r: represents the rhombohedra phase).

Fig. 3. XRD patterns of the pellets of 1Yb10ScSZ, obtained at room temperature, 300 °C, 400 °C, 450 °C and 500 °C (r: represents the rhombohedra phase).

Fig. 4. Dependence of the unit cell parameter on composition for the $(Yb_2O_3)_x$–$(Sc_2O_3)_{(0.11-x)}$–(ZrO_2) 0.89 ($x = 0$–0.11) system at room temperature.

the relative contributions of the bulk, grain boundary and electrode resistances. Fig. 5 presented the impedance spectra for 11ScSZ, 1Yb10ScSZ and 2Yb9ScSZ at 400 °C. The Fitted responses were also provided in the picture. The spectra had been interpreted with the aid of the parallel connected resistor-capacitor equivalent circuit, where high and intermediate frequency semicircles were related to bulk and grain boundary resistances, respectively, while the low frequency semicircle was attributed to electrode response. As can be seen in Fig. 5, the relative contribution of bulk, grain boundary and electrode resistance varied with Yb content. The bulk resistance was calculated from the high frequency intercept because it could not be observed at higher temperatures [23]. With increasing temperature, bulk and grain boundary resistances both
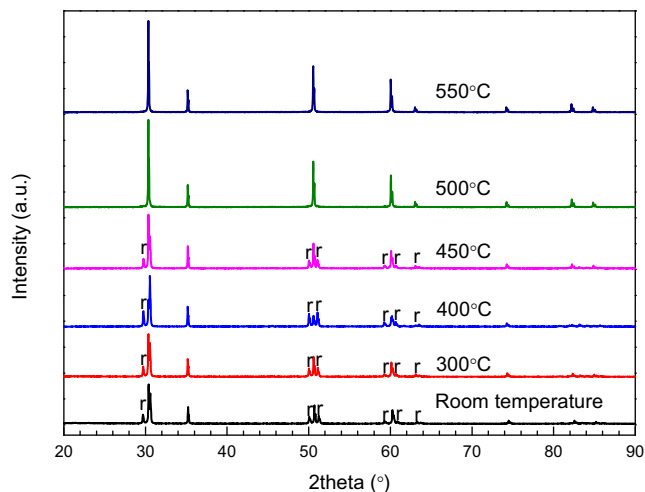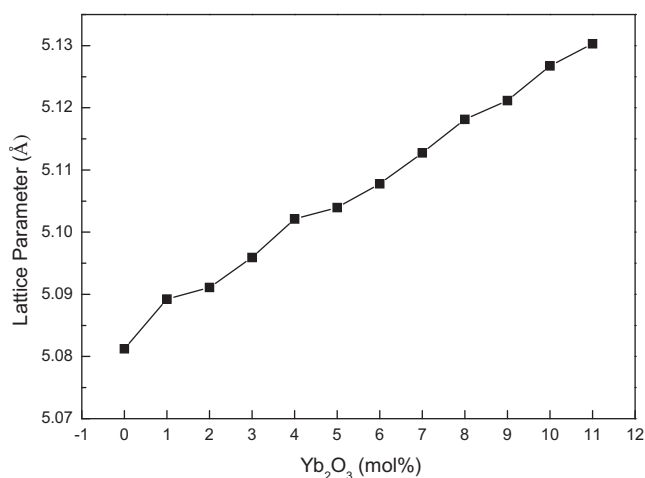
decreased and the contribution from grain boundary decreased for all samples. In higher temperature region, the grain boundary resistance disappeared, and the electrical conductivity was merely attributed to bulk resistance. At lower temperature, the grain boundary resistance dominated the electrical transportation of 11ScSZ [17]. We took the first intermediate frequency circle as the grain boundary resistance for the 11ScSZ sample. Comparing to the 11ScSZ, the grain boundary resistance was apparently reduced both for 1Yb10ScSZ and 2Yb9ScSZ. The bulk and grain boundary resistance of 2Yb9ScSZ were also smaller than the 1Yb10ScSZ, respectively. The total resistance of bulk and grain boundary declined with the addition of Yb_2O_3 in the range from 0% to 3 mol%. These suggested that the electrical properties can be improved at lower temperature with doping Yb_2O_3.

The activation energy values of all compositions were calculated using the Arrhenius equation as expressed in Eq. (1):

$$\sigma T = A \exp(-H/RT) \qquad (1)$$

where σ denoted the ionic conductivity, T the temperature in Kelvin, A the pre-exponential factor, H the activation enthalpy and R the gas constant. The parameters R take contributions from both the grain boundaries and the bulk into account.
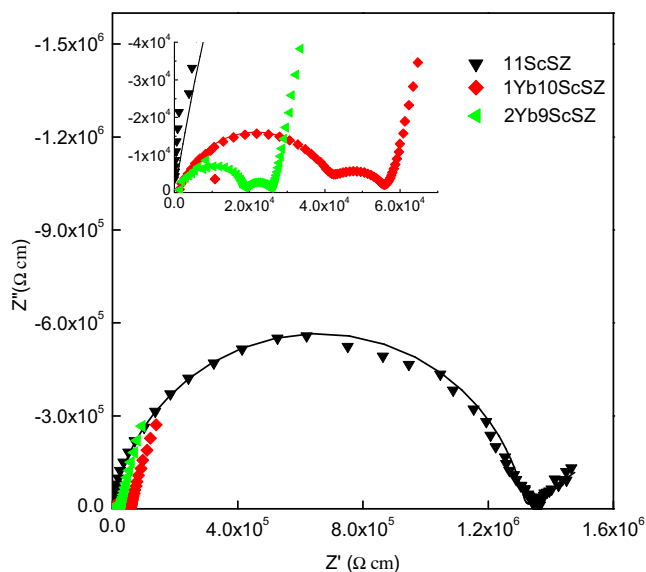
Fig. 5. Impedence spectra of 11ScSZ, 1Yb10ScSZ and 2Yb9ScSZ measured at 400 °C and the dark line is the fitted responses. (Inset) Drawing of partial enlargement for the same position, same color code.
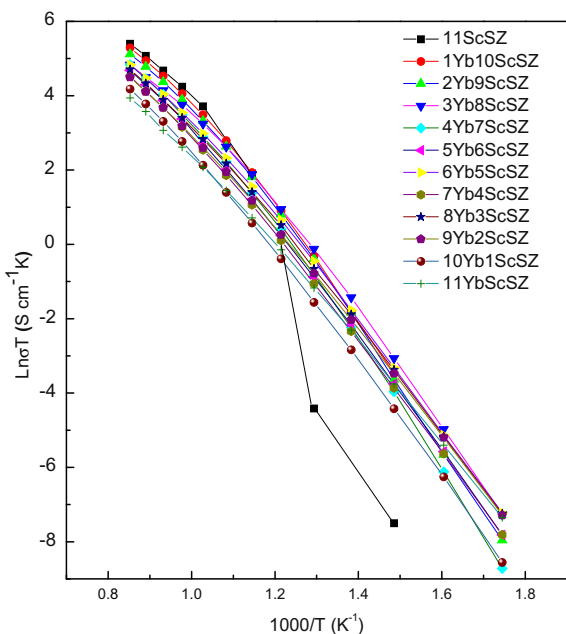

Fig. 6. Temperature dependence of ionic conductivity for the $(Yb_2O_3)_x$–$(Sc_2O_3)_{(0.11-x)}$–$(ZrO_2)_{0.89}$ ($x = 0$–0.11) system.

Fig. 7. Dependence of conductivity on composition for the $(Yb_2O_3)_x$–$(Sc_2O_3)_{(0.11-x)}$–$(ZrO_2)_{0.89}$ ($x = 0$–0.11) system at different temperatures.

The Arrhenius dependencies for all of the compositions according to Eq. (1) were shown in Fig. 6. The Arrhenius plots showed a curvature for all compositions from 300 °C to 900 °C. The samples gave a smooth curve except for the 11ScSZ, which displayed a discontinuity at 600 °C. According to the literature [10,12,13], the discontinuity in the Arrhenius plots arose from the phase transition from rhombohedral to cubic. As was well known, the rhombohedral phase was a low conductive phase [4]. When it transformed to the highly conductive cubic phase, there was an enhancement of the conductivity, and a discontinuity appeared in the Arrhenius plot. The discontinuity of the 11ScSZ sample was appeared in Fig. 6 and the rhombohedral phase was also analyzed by the XRD measurement at room temperature. Together with the in-situ XRD
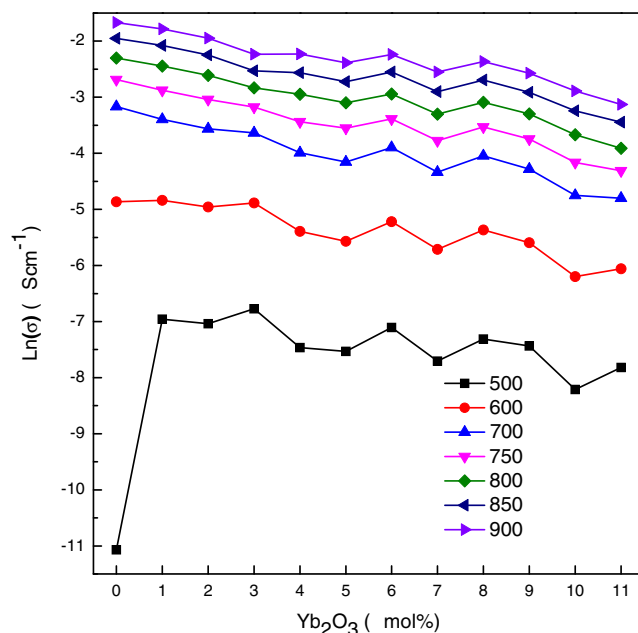
results of 1Yb10ScSZ whose rhombohedral phase transformed into cubic phase around 450–500 °C. The discontinuity of the 11ScSZ sample was probably caused by the phase transition.

The typical transformation temperature from rhombohedral to cubic phase occurred at around 600 °C [12]. In this study, a small amount of the rhombohedral phase was detected by XRD in some samples, such as 4Yb7ScSZ and 6Yb5ScSZ. However, no conductivity discontinuities were observed. For those compositions, the phase transition possibly took place below 400 °C, which is beyond the measured region 400–900 °C. The results of conductivity did not present discontinuities. Similar results had been observed in other reports. Chiba et al. [3] found that the transition temperature from the rhombohedral phase to the cubic phase shifted to a lower temperature region as the content of Yb_2O_3 increased. In Ota's experiment [20], the phase transition temperature also shifted to a low temperature region when the content of Ga_2O_3 was increased. Even for 1Yb10ScSZ, the discontinuities in conductivity were not observed, though an obvious rhombohedral phase can be seen in the XRD pattern. All this results showed that the substitution of Yb_2O_3 for Sc_2O_3 improved the conductivity of doped zirconia in the low temperature region. Even the addition of 1 mol% Yb_2O_3, which was not sufficient to stabilise the cubic phase to room temperature, also played an important role in enhancing the low temperature conductivity properties.

The dependence of conductivity on composition in the temperature range from 500 °C to 900 °C is shown in Fig. 7. In the high temperature region from 700 °C to 900 °C, the conductivities moderately decreased as the content of Yb_2O_3 increased. The sample of 11ScSZ showed the highest conductivity, 0.099 S/cm, whereas the 11YbScSZ achieved only 0.020 S/cm at 800 °C. In the low temperature region from 500 °C to 650 °C, the conductivities maintained almost a constant value before 3 mol% of Yb_2O_3 and then decreased gradually as the content of Yb_2O_3 increased. All the compositions containing Yb_2O_3 showed a higher conductivity than 11ScSZ at 500 °C. These indicated that the addition of Yb_2O_3 can improve the conductivity at low temperature by stabilizing the cubic phase. As is well known, 0.01 S/cm is the threshold value for application as an electrolyte. All of the compositions that contained Yb_2O_3 could maintain 0.01 S/cm at 700 °C in our experiment. The

2Yb9ScSZ and 3Yb8ScSZ compositions could even achieve 0.015 S/cm at 650 °C. At high temperature, the decrease in ionic conductivity with increasing Yb$_2$O$_3$ content is in agreement with the results for the (Y$_2$O$_3$)–(Sc$_2$O$_3$)–(ZrO$_2$) system with 11 mol% stabiliser reported in Ref. [12]. At high temperature, all compositions are cubic phase. The oxygen vacancy transports in the similar structure. This phenomenon can be explained mainly by the ionic size mismatch. The ionic radius of the Yb^{3+} is larger than that of the Sc^{3+}, which causes a greater strain energy and also enhances the steric hindrance for the free migration of vacancies [24], and thus gives rise to a decrease of the conductivity with increasing content of Yb^{3+}. While in the low temperature region, the improvement in conductivity by substitution of Yb^{3+} for Sc^{3+} can be explained by the contribution of the cubic phase stabilisation. As is well known, there was negative correlation between the conductivity and the activation energy. The main explanation for conductivity was described in detail at the next part for the activation parameters.

We know that beside the conductivity, volume changes will occur with this phase transition during the temperature up and down. And material can be broken down by volume changes. However two-phase behaviour is normally observed for 11ScSZ, this phase transition from rhombohedral to cubic is quite difficult to prevent. Chiba et al. [3] reported that 2 mol% Yb$_2$O$_3$ was sufficient to stabilise the cubic structure at room temperature. Though a small amount of the rhombohedral phase was observed in our experiment after the addition of Yb$_2$O$_3$, there was no negative effect on the conductivity in the low temperature regime. Comparing with 11ScSZ material, substituting the scandia with ytterbium leads to a lower conductivity at high temperatures, but, at the same time, it prevents the phase transition from occurring at low temperatures. In addition, the decrease in the conductivity of 2Yb9ScSZ was slightly lower than that of the sample of 11ScSZ in the high temperature range from 700 to 1000 °C, which is the typical operation temperature range for SOFCs. Thus, this system is very promising for the application as an electrolyte material.

4.2. Activation parameters

It is known that the oxygen vacancies were induced by doping of ZrO$_2$ with aliovalent cations as charge compensating defects. The defect formation reaction can be written in Kroger and Vink notation:

$$Yb_2O_3 \rightarrow 2Yb'_{Zr} + V\ddot{O} + 3O_o^{\times} \tag{2}$$

$$Sc_2O_3 \rightarrow 2Sc'_{Zr} + V\ddot{O} + 3O_o^{\times} \tag{3}$$

Due to the coulombic attraction caused by the effective charges in the lattice, together with the cation polarisability and the strain energy caused by the different sizes of the host and dopant cations, complex defect associations can be formed among dopants and the oxygen vacancies. However, the oxygen ion diffusion at high temperatures in the ZrO$_2$ solid solution may be mainly due to the free oxide ion vacancies. There have been many models proposed to calculate the activation energy [25–27]. In the low temperature region, the activation energy is composed of the oxygen vacancy migration energy (E_m) and association energy (E_{ass}). Kilner and Brook [26] suggested that the value of E_m depends more on the structure than on the host cation size. The variation of E_m is dependent upon the cation type in an isostructural series. The E_{ass} are strongly dependent on the dopant cation size, and a minimum may occur when the radius of the dopant equals that of the host. Mogensen et al. [25] argued that lattice distortion (lattice stress and deviation from cubic symmetry) due to the ion radius mismatch is of great importance. The vacancy mobility seems to be optimised when the deviations from the matching radius are

minimised and the cubic lattice has lower strains and distortions because the crystal symmetry is maximised and the vacancy–lattice interaction is minimised.

It is widely assumed that, at sufficiently high temperatures, the complex defect associations are completely dissociated and the isolated oxygen vacancies can migrate freely. According to this model, at low temperatures, the activation energy has a significant contribution from association, while, at high temperatures, the activation energy is equal to only the migration enthalpy. The diffusion of oxygen vacancies is affected by the elastic strain energy, which is related to the size mismatch between the host and dopant cations. Thus, the proposed model should be modified by the elastic strain energy. In our experiment, we selected the prior model for calculation. We assumed that the oxygen vacancies can migrate freely at high temperatures, and the migration mainly depends on the migration energy. We extracted the migration energy at a relatively high temperature where some associations may still exist as a subdominant role. In the low temperature regime, the activation energy comprises the oxygen vacancy migration energy (E_m) and the association energy (E_{ass}). It can be expressed as follows:

$$\text{Low temperature region}: \quad E_a = E_{ass} + E_m \tag{4}$$

$$\text{High temperature region}: \quad E_a = E_m \tag{5}$$

For the low temperature region 400–500 °C and 400–550 °C, we calculated the activation energy according to Eq. (1), (4) and (5):

$$E_{ass(400–500)} = E_{a(400–500)} - E_{a(800–900)}; \tag{6}$$

$$E_{ass(400–550)} = E_{a(400–550)} - E_{a(750–900)} \tag{7}$$

The apparent association energy can be obtained from impedance data for the difference between the high and low temperature activation energies, which is illustrated in Fig. 8, which shows a plot of the migration energy and association energy as a function of specimen composition in the temperature ranges 400–500 °C and 400–550 °C. Correspondingly, the activation energy was obtained from the impedance data in the temperature ranges 400–500 °C, 400–550 °C, 800–900 °C and 750–900 °C.

As shown in Fig. 8, the migration energy increased and the association energy decreased with an increasing content of Yb$_2$O$_3$. It is well known that the conductivity is negatively correlated with the activation energy. In agreement with the conductivities results in Fig. 8, the E_m at 400–500 °C and 400–550 °C, increased when the content of Yb$_2$O$_3$ increased, corresponding to the E_a in the high
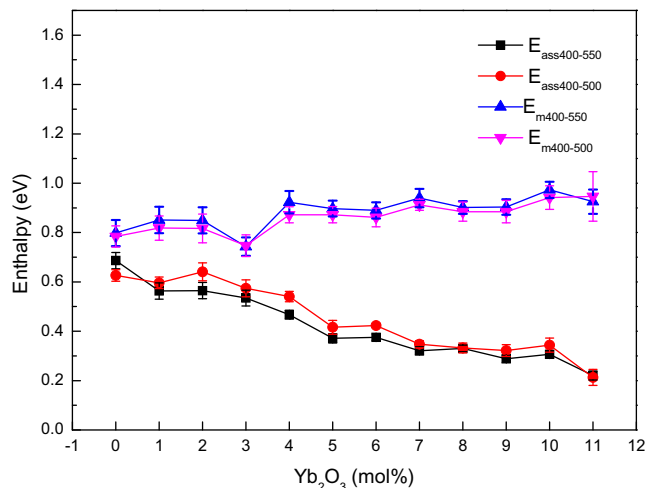

Fig. 8. Dependence of the activation enthalpy on composition for the (Yb$_2$O$_3$)$_x$–(Sc$_2$O$_3$)$_{(0.11-x)}$–(ZrO$_2$)$_{0.89}$ (x = 0–0.11) system at different temperatures.

temperature regions 800–900 °C and 750–900 °C. The conductivity decreased with increasing migration energy at high temperature. A similar phenomenon was observed in the Y_2O_3–Sc_2O_3–ZrO_2 system [11,12] and the Ga_2O_3–Sc_2O_3–Zr_2O_3 system [20].

The association energy arises from the coulombic attraction (vacancy and dopant cation), strain energy (ionic radius mismatch, structural distortion) and steric blocking and may also include some other blocking energy, such as the hindrance energy caused by local ordering [28–30]. On the basis of the experimental results, we suggest that a majority of associations disassociate at high temperature, yet the steric blocking and strain energy caused by ionic size differences still exist and come to play the dominant role. They twist the oxygen path, create energy hindrances and finally lead to low conductivity. Because the radius of Yb^{3+} is larger than that of Sc^{3+}, the larger migration energy can thus be expected for high Yb_2O_3 contents.

As the system Y_2O_3–Sc_2O_3–ZrO_2 [11,12] and Ga_2O_3–Sc_2O_3–Zr_2O_3 [20] mentioned above, no matter the ionic radius is larger than that of Zr^{4+} or not, the association energy in the ternary system decreased compared to that of the binary system at low temperatures. As Fig. 8 shows the association energy decreased with the increase of Yb_2O_3 content. And slight addition of the other oxide dopant could improve the conductivity. In our research, the conductivity just showed a trivial increase at 500 °C before 3 mol% Yb_2O_3 which is shown in Fig. 7. All this may indicate that, by complex doping, we can lower the association energy at lower temperature. Compositions that distort the crystal structure less by complex doping could lead to very promising materials for low temperature operation of SOFCs.

5. Conclusion

The co-precipitation synthesised samples of the ternary system $(Yb_2O_3)_x$–$(Sc_2O_3)_{(0.11-x)}$–$(ZrO_2)_{0.89}$ ($x = 0$–0.11) were studied. The cubic phase was obtained by the substitution of Yb_2O_3 for Sc_2O_3 except for the 1Yb10ScSZ sample, which contained the rhombohedral phase. The conductivity decreased gradually in the temperature region from 800 °C to 900 °C with increasing Yb_2O_3 content. However, in the low temperature region from 500 °C to 600 °C, the conductivity remained at almost the same value when the content of Yb_2O_3 was less than 3 mol% and then gradually decreased with increasing Yb_2O_3. As for 2Yb9ScSZ and 3Yb8ScSZ compositions, the ionic conductivity of 0.015 S/cm was achieved at 650 °C. The addition of Yb_2O_3 decreased the association enthalpy and increased the migration enthalpy. The strain energy and steric blocking effect arose from the ionic radius difference should account for this migration enthalpy increase. Based on the consideration of the phase structure, conductivity properties and cost of raw materials, 3Yb8ScSZ is a potential electrolyte candidate for applications at low intermediate temperatures.

Reference

[1] B. Lin, S. Wang, X. Liu, G. Meng, J. Alloys Compd. 490 (2010) 214.
[2] Y. Mizutani, K. Hisada, K. Ukai, H. Sumi, M. Yokoyama, Y. Nakamura, O. Yamamoto, J. Alloys Compd. 408–412 (2006) 518.
[3] R. Chiba, T. Ishii, F. Yoshimura, Solid State Ionics 91 (1996) 249.
[4] S.P.S. Badwal, F.T. Ciacchi, D. Milosevic, Solid State Ionics 136–137 (2000) 91.
[5] K. Nomura, Y. Mizutani, M. Kawai, Y. Nakamura, O. Yamamoto, Solid State Ionics 132 (2000) 235.
[6] D.-S. Lee, W.S. Kim, S.H. Choi, J. Kim, H.-W. Lee, J.-H. Lee, Solid State Ionics 176 (2005) 33.
[7] M. Liu, C. He, J. Wang, W.G. Wang, Z. Wang, J. Alloys Compd. 502 (2010) 319.
[8] Z. Wang, M. Cheng, Z. Bi, Y. Dong, H. Zhang, J. Zhang, Z. Feng, C. Li, Mater. Lett. 59 (2005) 2579.
[9] N. Orlovskay, S. Lukich, G. Subhash, T. Graule, J. Kuebler, J. Power Sources 195 (2010) 2774.
[10] E. de Carvalho, W. Preis, W. Sitte, J.T.S. Irvine, Solid State Ionics 181 (2010) 1344.
[11] F.T. Ciacchi, S.P.S. Badwal, J. Eur. Ceram. Soc. 7 (1991) 197.
[12] T.I. Politova, J.T.S. Irvine, Solid State Ionics 168 (2004) 153.
[13] S.P.S. Badwal, F.T. Ciacchi, S. Rajendran, J. Drennan, Solid State Ionics 109 (1998) 167.
[14] H. Yamamura, N. Utsunomiya, T. Morib, T. Atakec, Solid State Ionics 107 (1998) 185.
[15] D. Meyer, U. Eisele, R. Satet, J. Rödel, Scr. Mater. 58 (2008) 215–218.
[16] H. Yamamura, T. Matsusita, H. Nishino, K. Kakinuma, J. Mater. Sci. – Mater. Electron. 13 (2002) 57.
[17] B. Bai, N.M. Sammes, A.L. Smirnova, J. Power Sources 176 (2008) 76.
[18] A. Yamaji, T. Koshikawa, W. Araki, T. Adachi, J. Eng. Mater. 131 (2009) 011010.
[19] T. Ishii, Solid State Ionics 78 (1995) 333.
[20] Y. Ota, M. Ikeda, S. Sakuragi, Y. Iwama, N. Sonoyama, S. Ikeda, A. Hirano, N. Imanishi, Y. Takeda, O. Yamamoto, J. Electrochem. Soc. 157 (2010) B1707.
[21] R. Ruh, H.J. Garrett, R.F. Domagala, V.A. Patel, J. Am. Ceram. Soc. 60 (1977) 399.
[22] Y. Zhang, X. Sun, G. Xu, C. Yan, Solid State Sci. 6 (2004) 523.
[23] I. Kosacki, H.U. Anderson, Y. Mizutani, K. Ukai, Solid State Ionics 152–153 (2002) 431.
[24] R.J. Stafford, S.J. Rothman, J.L. Routbort, Solid State Ionics 37 (1989) 67.
[25] M. Mogensen, D. Lybye, N. Bonanos, P.V. Hendriksen, F.W. Poulsen, Solid State Ionics 174 (2004) 279.
[26] J.A. Kilner, R.J. Brook, Solid State Ionics 6 (1982) 237.
[27] Y. Arachi, H. Sakai, O. Yamamoto, Y. Takeda, N. Imanishai, Solid State Ionics 121 (1999) 133.
[28] M. Burbano, S.T. Norberg, S. Hull, S.G. Eriksson, D. Marrocchelli, P.A. Madden, G.W. Watson, Chem. Mater. 24 (2011) 222.
[29] T. Mori, T. Ikegami, H. Yamamura, J. Electrochem. Soc. 146 (1999) 4380.
[30] C. Jiménez-Solís, L. Esquivias, C. Prieto, J. Alloys Compd. 228 (1995) 188.